Separation and Purification Technology 382 (2026) 135918

Contents lists available at ScienceDirect

Separation and Purification Technology

journal homepage: www.elsevier.com/locate/seppur

Potato-chip-like two-dimensional magnetic trimetallic oxides derived from MXene-MOF nanocomposites for fast enrichment of phosphopeptides

Sen Zhang [a], Xingdong Yang [a], Feng Zhang [a], Jun-qin Qiao [a], Wei-juan Zheng [b], Hong-zhen Lian [a,*]

[a] State Key Laboratory of Analytical Chemistry for Life Science, School of Chemistry & Chemical Engineering and Center of Materials Analysis, Nanjing University, 163 Xianlin Avenue, Nanjing 210023, China

[b] State Key Laboratory of Pharmaceutical Biotechnology, School of Life Sciences, Nanjing University, 163 Xianlin Avenue, Nanjing 210023, China

ARTICLE INFO

Keywords:
MXene-MOF nanocomposites
$Ti_3C_2T_x$ MXene
UiO-66–NH_2
Magnetic trimetallic oxides
Metal oxide affinity chromatography (MOAC)
Phosphopeptides enrichment
Traditional Chinese medicine injections (TCMIs)

ABSTRACT

Both MXenes and metal-organic frameworks (MOFs) have been attracting lots of attention since being found and have been applied in various fields. Furthermore, MXene-MOF composites have been recently studied to combine the advantages of MXenes and MOFs. However, the synthesis of MXene-MOF composites still suffers from questions such as low-efficiency of exfoliation of MXenes to layered nanosheets, uneven distribution of MOF nanoparticles on MXene nanosheets and extra modification process before the growth of MOF nanoparticles. To resolve these problems, herein, a sonication-assisted minimally intensive layer delamination (SA-MILD) method was proposed to achieve high yield of thin-layer $Ti_3C_2T_x$ MXene nanosheets. Then, a stirring in-situ growth method (SISG) was carried out to uniformly grow UiO-66–NH_2 nanoparticles on $Ti_3C_2T_x$ nanosheets to form two-dimensional potato-chip-like Ti_3C_2–UiO-66–NH_2 nanocomposites instead of conventional solvothermal method for the first time. Finally, MXene-MOF composites were calcined to increase the chemical stability and endowed with magnetism by the in-situ oxidation growth of Fe_3O_4 nanoparticles. Thanks to the massively exposed Ti—O, Zr—O and Fe—O sites, the well-characterized magnetic trimetallic oxides (MTMOs) could enrich phosphopeptides by easy magnetic separation through metal oxide affinity chromatography mechanism in a short time. High sensitivity (0.5 nmol•L^{-1} of $\alpha-/\beta$-casein) and great anti-interference ability (1:1:2000 of the molar ratio of $\alpha-/\beta$-casein to bovine serum albumin) were realized for the efficient enrichment of phosphopeptides with MTMOs. Non-fat milk and traditional Chinese medicine injections were used as the examples to explore the biomedical applicability of the as-prepared MTMOs with excellent results.

1. Introduction

MXenes are a large family of two-dimensional (2D) metal carbides or nitrides produced by etching A layers from MAX phases, with a composition of $M_{n+1}X_nT_x$, where M stands for one or more early transition metals, A is mainly a group IIIA or IVA element, X is C and/or N and n = 1, 2, or 3 [1]. Benefitted from their unique characteristics, MXenes have received great attention since being found, and have been applied in diverse fields including energy storage, optoelectronics, sensors, biomedicines and so on [2]. Their large surface area and special surface properties endow them with promising application in separation science, which has been explored in the removal of Pb(II) [3], removal of methylene blue [4], water purification [5], extraction of uranium [6], etc.

Phosphorylation is one of the most important post-translational modifications of proteins, playing crucial roles in diverse biological and pathological processes, including cellular differentiation and proliferation, protein degradation, signal transduction, transcriptional regulatory, gene expression regulation and so on [7]. The abnormal phosphorylation of proteins is relevant to multiple diseases such as cancer [8], Alzheimer's disease [9], etc. In present, the analysis of protein phosphorylation depends highly on mass spectrometry (MS) based on bottom-up strategies. Matrix assisted laser desorption/ionization time-of-flight mass spectrometry (MALDI-TOF MS) has been widely employed to identify phosphopeptides/phosphoproteins on account of its ultrahigh sensitivity, high-throughput, dynamic range, and fast analysis speed [10]. Nevertheless, signals of phosphopeptides are usually low resulted by their low deionization efficiency and the

* Corresponding author.
E-mail address: hzlian@nju.edu.cn (H.-z. Lian).

https://doi.org/10.1016/j.seppur.2025.135918
Received 23 September 2025; Received in revised form 25 October 2025; Accepted 30 October 2025
Available online 1 November 2025

suppression from non-phosphopeptides of higher abundance [11]. Therefore, it is of great necessity to enrich glycopeptides from the sample prior to detection by MALDI-TOF MS [12].

To date, the strategies to enrich phosphopeptides/phosphoproteins include immunoprecipitation [13], ion exchange chromatography [14], immobilized metal affinity chromatography (IMAC) [15], metal oxide affinity chromatography (MOAC) [16], etc. Among all these approaches, MOAC has been widely employed for the advantages of MOAC materials such as good mechanical stability, strong resistance to extreme pH and temperature, maintaining of metal ions [17], etc.

Currently, there are only a few reports on the enrichment of phosphopeptides/phosphoproteins with MXene related materials. Ou's group [18] first investigated the performance of Ti_3AlC_2 MAX phase and $Ti_3C_2T_x$ MXene phase in enrichment of phosphopeptides. Lan and Wu's group [19] partially oxidized and modified $Ti_3C_2T_x$ MXene with amino groups and fabricated $Fe_3O_4/TiO_2@Ti_3C_2T_x$ by a solvothermal method. They [20] also functionalized $Ti_3C_2T_x$ MXene with polyamidoamine (PAMAM) dendrimer and Fe_3O_4 nanoparticles to form $Ti_3C_2T_x$@PAMAM@Fe_3O_4. In their another work [21], dielectric barrier discharge (DBD) was used to rapidly synthesize Oxid-$Ti_3C_2T_x$/UiO-66–NH_2 composites. Our previous work [22] prepared Ti_3C_2–Fe_3O_4 by an in-situ oxidation growth method in water solution at room temperature. Yu and Wu's group [23] prepared a metal-phenolic networks modified magnetic MXene based composites $Ti_3C_2T_x@Fe_3O_4@$MPNs-TA/Zr^{IV}. Li and Liang's group [24] in situ oxidized $Ti_3C_2T_x$ MXene to synthesize polycrystalline TiO_2 on the surface of the nanosheets to form $Ti_3C_2T_x$-O.

Among these various modifications on MXenes adopted to enhance the performance enriching phosphopeptides/phosphoproteins, modification with metal-organic frameworks (MOFs) provides researchers with new thoughts and possibilities. MOFs are porous crystalline frameworks by linking metal centers and organic ligands to form infinite arrays. They have been drawing growing interests owing to their special properties, such as extremely high porosity, massive surface area, tunable pore size distribution, and so on [25–28]. In the vast family of MOFs, zirconium-based MOFs, with a metal center of Zr, are attracting researchers' attention due to their uniform adjustable structure, incomparable biocompatibility, good chemical stability brought by strong Zr—O bonds and large coordination numbers [29,30], etc. However, the growth of Zr-based MOFs such as UiO-66 and UiO-66–NH_2 on MXenes is still facing challenges. The major solution is solvothermal method to grow Zr-based MOFs on MXenes. For example, Li and Pan's group [31] grew UiO-66 nanoparticles on V_2CT_x and obtained UiO-66/V_2CT_x composites and then derived them for an anode for lithium-ion batteries. Wang and Gao's group [32] synthesized Ti_3C_2/UiO-66–NH_2 composites for photoreduction of Cr(VI). Li and Liu's group [33] also synthesized MXene-MOF composites named UN@Ti_3C_2 and derived UN@Ti_3C_2 for electrochemical detection of acetaminophen. Hasanzadeh's group [34] prepared $Ti_3C_2T_x$ MXene@UiO-66 for photocatalytic dye degradation. Deng's group [35] fabricated a UiO-66–NH_2@MXene for H_2/CO_2 separation. These MXene-MOF composites, however, suffer from one or more questions: (1) MXenes are not delaminated into thin layers in the composites; (2) distribution of the MOFs nanoparticles is not uniform enough; (3) modification of the $Ti_3C_2T_x$ surface is needed to form composites. Though Lan and Wu's group [21] synthesized evenly distributed UiO-66–NH_2 on delaminated $Ti_3C_2T_x$ nanosheets using DBD technology considering these factors, the size of MOF nanocrystals was somewhat large and comparable to that of the nanosheets. Additionally, the reaction required a dedicated DBD device.

In order to overcome the insufficiency, in this present work, we developed a stirring in-situ growth (SISG) strategy for the modification of UiO-66–NH_2 nanoparticles on thin-layer $Ti_3C_2T_x$ nanosheets prepared by a sonication-assisted minimally intensive layer delamination (SA-MILD) method to form uniformly distributed potato-chip-like 2D nanocomposites. The 2D MXene-MOF composites were then derived into metal oxides by calcination, increasing the chemical stability and maintaining the 2D structure and massive functional Ti—O and Zr—O sites on the nanosheets. Moreover, magnetism was endowed to the 2D nanocomposites by the in-situ oxidation growth of Fe_3O_4 nanoparticles. The 2D magnetic trimetallic oxides (MTMOs) nanosheets were then applied as a magnetic solid-phase extraction (MSPE) adsorbent in the fast enrichment of phosphopeptides through MOAC mechanisms benefitted from the abundant Ti—O, Zr—O and Fe—O sites. Ultimately, complex samples including non-fat milk and traditional Chinese medicine injections (TCMIs) were employed for investigate the practicability and reliability of MTMOs bio-separation in real world.

2. Experimental section

2.1. Materials and chemicals

Ti_3AlC_2 (400 mesh) was bought from RHAWN (Shanghai, China). $ZrCl_4$, 2-amino-1,4-benzenedicarboxylic acid (NH_2–BDC, 98%), 1,4-benzenedicarboxylic acid, *N*,*N*-dimethylformamide (DMF), ammonia solution (25–28%), acetic acid (HAc, 99.5%) and LiF were purchased from Macklin (Shanghai, China). Hydrochloric acid (35%–37%) was obtained from Sinopharm Chemical Reagent Co., Ltd. (Shanghai, China). $FeSO_4 \bullet 7H_2O$, disodium 4-nitrophenylphosphate (pNPP), 2,5-dihydroxybenzoic acid (DHB, HPLC grade), acetonitrile (ACN, HPLC grade), trifluoroacetic acid (TFA, HPLC grade) and H_3PO_4 (85%) were bought from Aladdin (Shanghai, China). Bovine serum albumin (BSA), α-casein from bovine milk, β-casein from bovine milk and trypsin from bovine pancreas (TPCK treated) were bought from Sigma-Aldrich (St. Louis, MO, USA). All the chemicals were of analytical grade unless otherwise stated and could be used without further purification. Pure water was prepared with a Milli-Q water purification system (Millipore, Billerica, MA, USA). Standard phosphopeptide LRRA[*pS*]LGGK was purchased from Sangon Biotech (Shanghai, China). Non-fat milk was purchased at Jiangsu Province Educational Supermarket (Nanjing, China). TCMIs Qingkailinng injection (QKLI) and Reduning injection (RDNI) were provided by Jiangsu Institute for Food and Drug Control (Nanjing, China).

2.2. Synthesis of potato-chip-like two-dimensional magnetic trimetallic oxides (MTMO)

The whole synthesis process of MTMO is illustrated in Scheme 1A.

Thin-layer $Ti_3C_2T_x$ MXene nanosheets were synthesized by a SA-MILD method based on conventional minimally intensive layer delamination (MILD) method [36]. First, 1.0 g Ti_3AlC_2 was added into 20 mL 9 mol•L^{-1} HCl solution containing 1.6 g LiF. The etching process was prolonged to 48 h at 40 °C. The resulted mixture was centrifugated for 1 min at 5000 rpm. Subsequently, the sediment was washed with 70 mL 2 mol•L^{-1} HCl once and then with 70 mL water each cycle until the supernatant was dark. Instead of hand-shaking, sonication of 5 min in an ice bath with a KQ218 ultrasonic cleaner (Kunshan Ultrasonic Instruments Co., Ltd., 100 W) was introduced in the washing step to accelerate the exfoliation of MXene nanosheets and at the same time save labor and time. After a few washing-centrifugation cycles, the supernatant turned dark, indicating that the pH of the dispersion has reached neutral and the delamination has been proceeding. Subsequently, three additional sonication-centrifugation cycles were performed without discarding the supernatant to further delaminate MXene to increase the yield. After a final centrifugation of 2000 rpm for 20 min, the MXene dispersion was collected and lyophilized for further use. Interestingly, this is the first time to put forward SA-MILD strategy to facilitate the exfoliation of $Ti_3C_2T_x$ MXene nanosheets. Compared to other post-etching delamination strategy [37], this high-yield strategy can save time and additional treatment steps.

Ti_3C_2–UiO-66–NH_2 was assembled by a SISG approach referring to the synthesis of UiO-66–NH_2 [38]. Lyophilized $Ti_3C_2T_x$ MXene nanosheets of a certain weight were dispersed in 10 mL DMF with sonication. Then a solution containing 5 mL DMF and 0.35 mmol $ZrCl_4$ and another

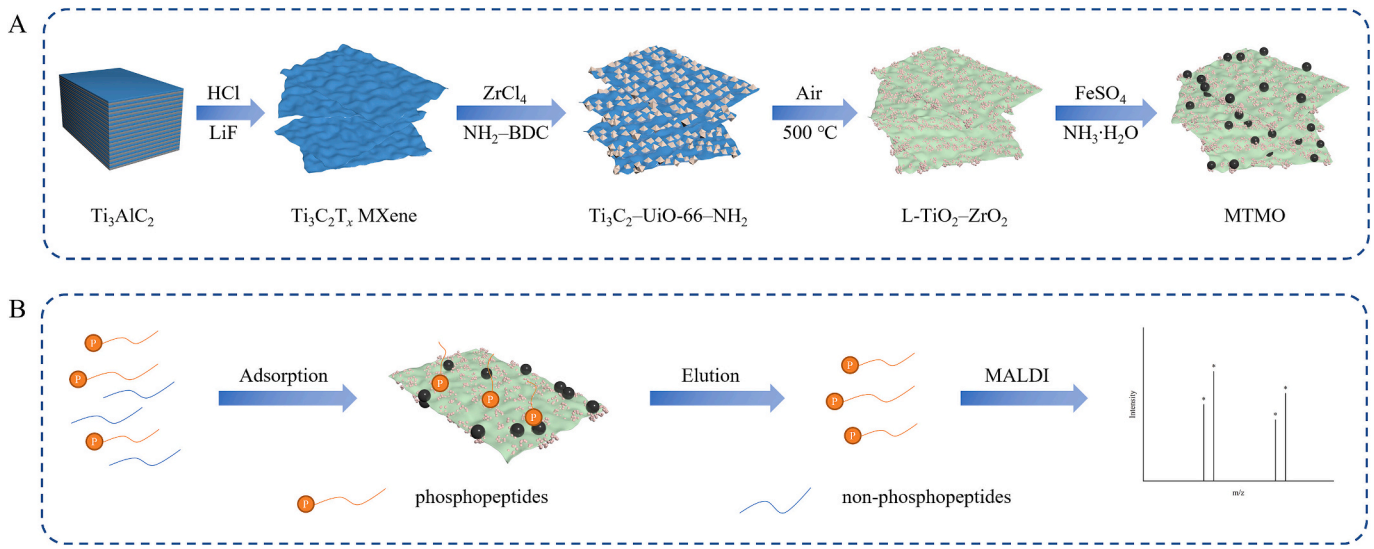

Scheme 1. Schematic diagram of the synthesis of MTMO (A), and the procedure of enriching phosphopeptides (B).

solution containing 5 mL DMF and 0.35 mmol NH_2–BDC were added into the $Ti_3C_2T_x$ dispersion, followed by 10 μL H_2O and 2 mL HAc. Instead of hydrothermal process, the mixture was magnetically stirred at 120 °C for 24 h. After that, the sediment was isolated, washed and collected by centrifugation. The amounts of Ti source and Zr source used for Ti_3C_2–UiO-66–$NH_{2(m/n)}$ are shown in Table S1, where *m/n* is the molar ratio of Ti source to Zr source (Ti/Zr).

The obtained Ti_3C_2–UiO-66–$NH_{2(m/n)}$ was calcined in air at 500 °C for 12 h, allowing the MXene-MOF composites to be oxidized into layered TiO_2-ZrO_2 composites (L-TiO_2–$ZrO_{2(m/n)}$). Then Fe_3O_4 nanoparticles were decorated onto the L-TiO_2–$ZrO_{2(m/n)}$ by an in-situ oxidation growth method. In brief, a solution containing $FeSO_4$ was added into a L-TiO_2–$ZrO_{2(m/n)}$ dispersion, followed by the addition of ammonia solution. Under the basic condition, the Fe^{2+} ions were partially oxidized to Fe^{3+} and formed Fe_3O_4 on the nanosheets. The final magnetic trimetallic oxides ($MTMO_{m/n}$) were collected after washing, and were dried in vacuum.

2.3. Characterization

Scanning electron microscopy (SEM) images of Ti_3AlC_2, $Ti_3C_2T_x$, Ti_3C_2–UiO-66–NH_2, L-TiO_2–ZrO_2 and MTMO were taken on a JSM-7800F field emission scanning electron microscope (JEOL, Tokyo, Japan). Transmission electron microscopy (TEM) images were taken and selected area electron diffraction (SAED) was performed on an FEI Tecnai G2F20S-TWIN microscope (FEI, Hillsboro, OR, USA) equipped with an Oxford X-Max80 X-ray energy dispersive spectrometer (EDS, Oxford Instruments, Abingdon, UK). X-ray diffraction (XRD) patterns were got on a Bruker D8 Advance X-ray powder diffractometer (Bruker, Karlsruhe, German) equipped with Cu Kα radiation, with an operating voltage of 40 kV and current of 40 mA. Raman spectra were collected on an inVia confocal Raman microscope using a 633 nm laser (Renishaw, Wotton-under-Edge, UK). Fourier-transform infrared (FT-IR) spectra were collected on a Nicolet iS50 FTIR spectrometer (Thermo-Fisher, Waltham, MA, USA) using KBr pellet method. X-Ray photoelectron spectra (XPS) were obtained on an ESCALAB 250 Xi XPS spectrometer (Thermo-Fisher, Waltham, MA, USA). Brunauer-Emmett-Teller (BET) surface area analysis was performed on an ASAP 2460 surface area and porosimetry system (Micromeritics, Norcross, GA, USA). The hysteresis loop of MTMO was measured on a Lake Shore 7604 vibrating sample magnetometer (Lakeshore, Carson, CA, USA). UV–vis spectra of pNPP solutions were recorded on a NanoDrop 2000 spectrophotometer (Thermo-Fisher, Waltham, MA, USA).

2.4. Sample preparation

The samples were prepared for phosphopeptides enrichment by MSPE on MTMO based on our previous work [23]. That is, 1 mg•mL^{-1} of α-casein, β-casein or BSA was dissolved in 100 mM NH_4HCO_3 and trypsin (1 mg•mL^{-1}) was added at a mass ratio of 1:40 (trypsin to protein). The mixture was incubated at 37 °C for 18 h, and then the digests were stored at −20 °C prior to enrichment. In concern about non-fat milk, 30 μL of non-fat milk was diluted with 1 mL 100 mM NH_4HCO_3 and centrifugated at 14000 rpm for 15 min. The supernatant was collected and 25 μg trypsin (25 μL, 1 mg•mL^{-1}) was added. After being incubated at 37° C for 18 h, the digests were kept at −20 °C before use. As for QKLI and RDNI, 10 mL of the injection was ultrafiltered in an ultra-15 centrifugal filter unit (Millipore, Billerica, MA, USA). After being washed with 100 mM NH_4HCO_3 for 3 times, the protein on the membrane was redissolved in about 1 mL 100 mM NH_4HCO_3. Then 10 μg trypsin (10 μL, 1 mg•mL^{-1}) was added and the mixture was incubated at 37 °C for 18 h. Centrifugal concentration to dryness ensued on a Labconco CentriVap Vacuum Concentrator (Labconco, Kansas City, MO, USA). The remnants were stored at −20 °C before use.

2.5. Enrichment of phosphopeptides

The workflow of enriching phosphopeptides is shown in Scheme 1B. In advance of the enrichment, α-casein and β-casein digests were mixed and diluted to 10^{-1} μmol•L^{-1}, non-fat milk digests were diluted 500 times, and the RDNI and QKLI remnants were re-dissolved in 1.0 mL with loading solution. Then, 5 μL of the dispersion of 20 mg•mL^{-1} MTMO was added to 100 μL of the sample solution. Subsequently, the mixture was vortexed at room temperature for 2 min. The resulting sediment was separated with the assistance of a magnet. After being washed with loading solution for 3 times, 5.0 μL of 10% NH_3•H_2O was added to elute the adsorbed phosphopeptides in a sonication bath for 1 min. The eluate was detected by MALDI-TOF MS.

2.6. Enrichment recovery of phosphopeptides

Two aliquots of standard phosphopeptides (LRRA[*pS*]LGGK) were separately labeled with light or heavy isotopes using CH_2O or CD_2O, causing a mass increase of 28 or 32 Da. The CH_2O-labeled phosphopeptide was then enriched with $MTMO_{3/4}$. The eluate was mixed with the same volume of CD_2O-labeled phosphopeptide and subjected to MS analysis. The ratio of the CH_2O-labeled phosphopeptide to the CD_2O-

labeled phosphopeptide was calculated to obtain the recovery of LRRA [*pS*]LGGK. At the same time, another CH_2O-labeled phosphopeptide before enrichment was mixed with CD_2O-labeled phosphopeptide and detected to eliminate the effects of the different labeling efficiency of CH_2O and CD_2O.

2.7. MALDI-TOF MS analysis

One microliter of the sample solution was dropped on an MTP 384 polished steel MALDI-TOF MS target plate (Bruker, Karlsruhe, German). After the solvent was vaporized to dryness, 1.0 μL DHB (20 mg•mL^{-1}) dissolved in 50% ACN – 1% H_3PO_4 was added as the matrix. The dried sample spots were analyzed on a Bruker ultrafleXtreme MALDI-TOF/TOF mass spectrometer (Bruker, Karlsruhe, German) with the Smartbeam-II laser technology in the positive reflection mode under an acceleration voltage of 25 kV. Each spectrum was accumulated to 500 shots.

3. Results and discussion

3.1. Synthesis and characterization of MTMO

SEM images of Ti_3AlC_2, $Ti_3C_2T_x$ MXene, Ti_3C_2–UiO-66–NH_2, L-TiO_2–ZrO_2 and MTMO are shown in Figs. 1A–D and S1–S5. It can be seen from these images that after SA-MILD process, with Al layers removed, the original bulky material (Fig. S1) was exfoliated into nanosheets (Figs. 1A and S2) with a silk-like surface. After in-situ growth of UiO-66–NH_2, the nanosheets showed a potato-chip-like morphology after the surface of Ti_3C_2 MXene nanosheets were covered by UiO-66–NH_2 nanoparticles (Figs. 1B and S3). Then after calcination in air, the structure of the potato-chip-like nanosheets didn't change, except that the relatively large particles of UiO-66–NH_2 on the surface of nanosheets broke into clusters of smaller particles (Figs. 1C and S4). Finally, larger nanospheres of Fe_3O_4 were modified onto the surface of the nanosheets (Figs. 1D and S5). TEM image of $MTMO_{3/4}$ shown in Fig. 1E reveals a clearer structure of nanosheets of TiO_2, nanoclusters of ZrO_2 and nanoparticles of Fe_3O_4. SAED patterns (Fig. 1F) exhibited the polycrystalline structure of TiO_2, ZrO_2 and Fe_3O_4 in $MTMO_{3/4}$. As shown in Fig. 1H–L, EDS mapping images of $MTMO_{3/4}$ corresponding to the area shown in Fig. 1G demonstrate the distribution of Ti, Zr and Fe, where Ti and Zr were uniformly distributed on the nanosheets and Fe was mainly on the nanoparticles.

In order to further confirm the synthesis of MTMO, some other characterization experiments were carried out. Fig. 2A shows XRD patterns of Ti_3AlC_2, $Ti_3C_2T_x$ MXene, Ti_3C_2–UiO-66–NH_2, L-TiO_2–ZrO_2 and MTMO. Before the etching and exfoliating, diffraction peaks of Ti_3AlC_2 localized at 2θ values of 9.6°, 19.1°, 34.0°, 38.7°, 41.7°, 44.8°, 48.4°, 52.3°, 56.3°, 60.2° and 65.3° corresponded respectively to the (002), (004), (100), (104), (105), (106), (107), (108), (109), (110) and (1,0,11) planes of Ti_3AlC_2. After SA-MILD treatment, most diffraction peaks of Ti_3AlC_2 disappeared, remaining the (110) peak at 60.6° and the (002) peak shifting to a lower angle of 6.5°, indicating a larger interlayer distance resulted by the intercalation of ions during the SA-MILD process. Other diffraction peaks at 21.6°, 38.1°, 41.0°, 42.4° and 48.3° were

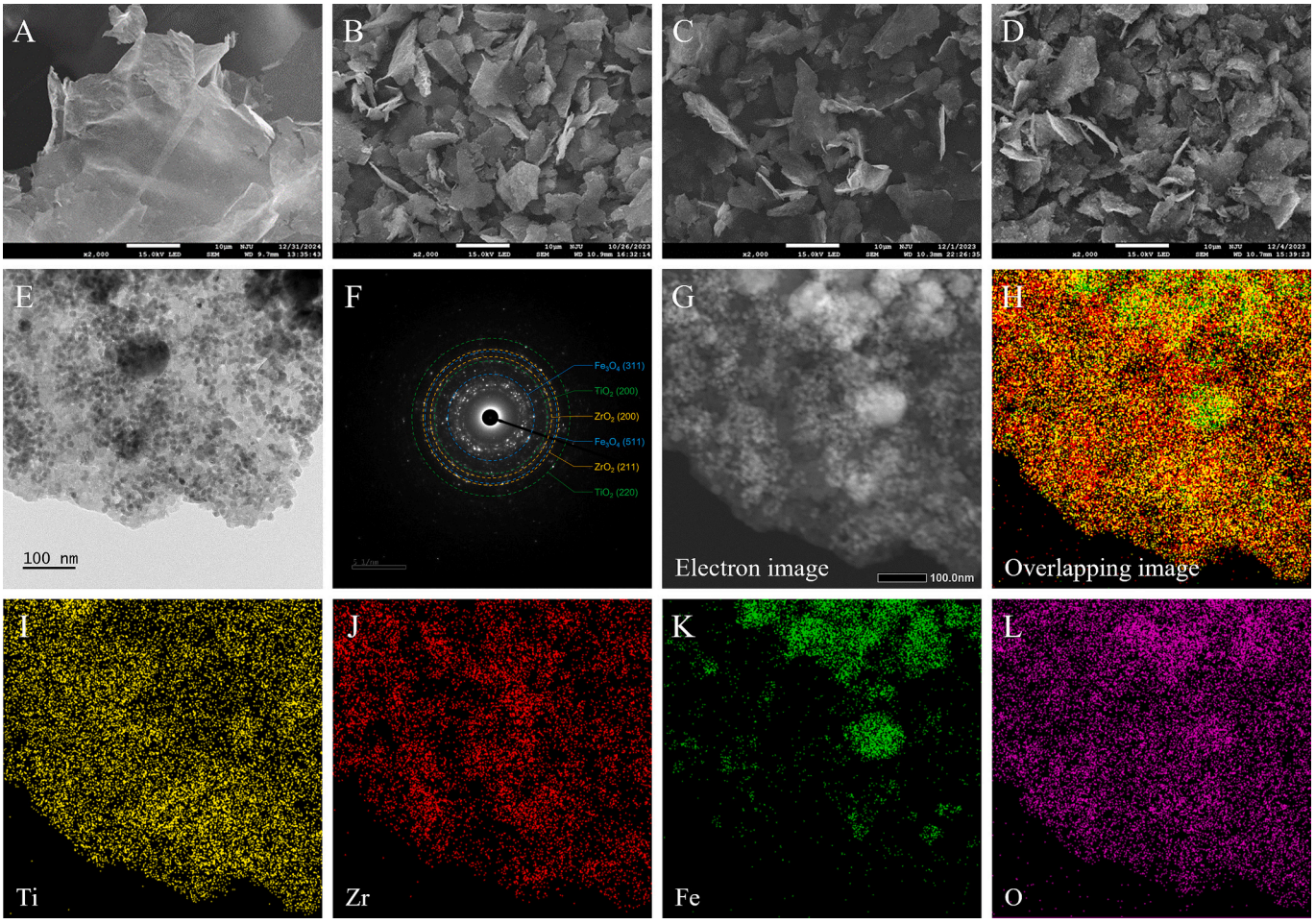

Fig. 1. SEM images of $Ti_3C_2T_x$ (A), Ti_3C_2–UiO-66–$NH_{2(3/4)}$ (B), L-TiO_2–$ZrO_{2(3/4)}$ (C) and $MTMO_{3/4}$ (D); TEM images of MTMO (E); SAED pattern of MTMO (F); TEM-EDS mapping of MTMO: electron image (G), overlapping image (H) and distribution images of Ti (I), Zr (J), Fe (K) and O (L).

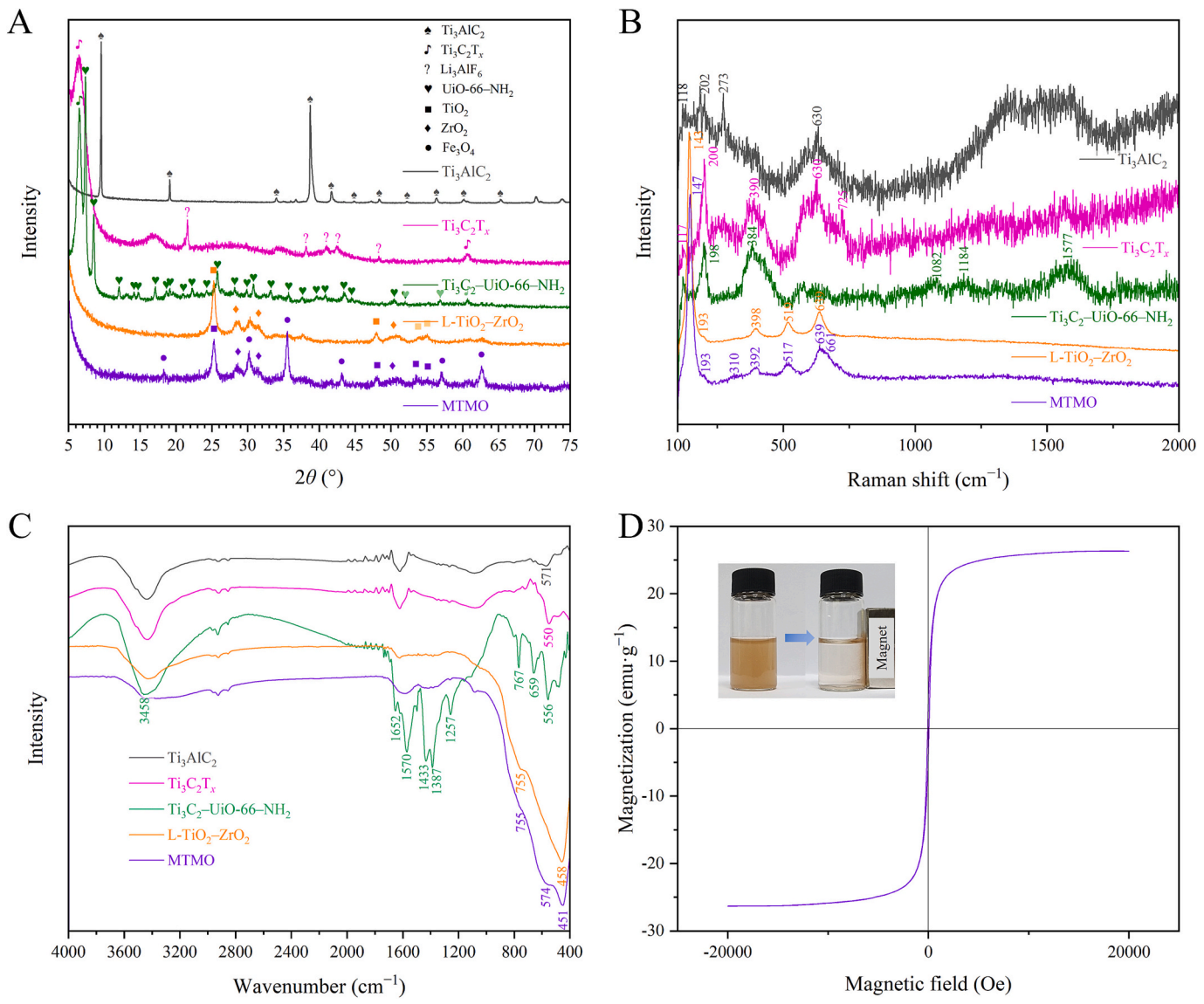

Fig. 2. XRD patterns (A), Raman spectra (B) and FT-IR spectra (C) of Ti_3AlC_2, $Ti_3C_2T_x$ MXene, Ti_3C_2–UiO-66–$NH_{2(3/4)}$, L-TiO_2–$ZrO_{2(3/4)}$ and $MTMO_{3/4}$, and hysteresis loop (D) of $MTMO_{3/4}$.

from the by-product Li_3AlF_6 remaining in the MXene nanosheets. As for Ti_3C_2–UiO-66–$NH_{2(3/4)}$, except for the (002) and (110) peaks of $Ti_3C_2T_x$, characteristic diffraction peaks confirmed the structure of UiO-66–NH_2, and the peaks of Li_3AlF_6 could no longer be seen. After calcination, due to the destruction of Ti_3C_2–UiO-66–NH_2, all their peaks disappeared and new peaks assigned to TiO_2 of anatase phase and ZrO_2 of baddeleyite phase were observed, indicating that in the presence of air, the MXene-MOF composites containing Ti and Zr were oxidized into oxides. And with the Fe_3O_4 nanoparticles decorated onto L-TiO_2–ZrO_2, peaks of Fe_3O_4 in the XRD pattern of MTMO were observed at 2θ values of 18.3°, 30.2°, 35.6°, 43.1°, 57.0° and 62.6°.

Raman and FT-IR spectra of Ti_3AlC_2, $Ti_3C_2T_x$ MXene, Ti_3C_2–UiO-66–NH_2, L-TiO_2–ZrO_2 and MTMO were measured to characterize the chemical bonds in these materials. As shown in Fig. 2B, Raman spectrum of Ti_3AlC_2 shows characteristic peaks at 118, 202, 273 and 630 cm^{-1}, ascribed to the in-plane vibration of Ti planes (E_{2g}), antiparallel shear vibration of Ti and Al planes (E_{2g}), out-of-plane vibration of Al (A_{1g}) and in-plane vibration of C (E_{2g}), respectively [39]. After SA-MILD process, the peak at 273 cm^{-1} assigning to the vibration of Al largely decreased, and other peaks at 117, 200 and 630 cm^{-1} remained in association with Ti and C, suggesting the removal of aluminum. Besides, new peaks at 390 and 725 cm^{-1} were observed, which came from the in-plane vibration (E_g) of the surface groups and the out-of-plane vibration of C (A_{1g}) with a larger interlayer spacing, respectively [40]. As for Ti_3C_2–UiO-66–NH_2, the peak at 384 cm^{-1} was ascribed to the vibration of Zr—O clusters merging with the peak of Ti—C, Ti—O and Ti—OH. And the peak around 1577 cm^{-1} was assigned to the stretching vibration of the aromatic rings in NH_2–BDC [41]. After being calcined in air, the spectrum of L-TiO_2–ZrO_2 show peaks at 143, 398, 519 and 639 cm^{-1}, corresponding to the typical E_g, B_{1g}, B_{2g} and E_g vibrations of anatase TiO_2. Meanwhile, as most of the peaks assigning to ZrO_2 were masked by or overlapped with the peaks of TiO_2, only one peak at 193 cm^{-1} observed was ascribed to ZrO_2 [42]. After the in-situ oxidation growth of Fe_3O_4, a weak peak at 310 cm^{-1} of the bending vibration of Fe (T_{2g}) and the expansion of the peak at 639 cm^{-1} caused by another peak at 661 cm^{-1} assigning to the symmetric vibration of Fe (A_{1g}) were observed. With respect to the FT-IR spectra (Fig. 2C), the spectrum of Ti_3AlC_2 shows a weak peak at 571 cm^{-1}, which were assigned to the stretching vibration of Ti—C bonds. The peak of Ti—C in $Ti_3C_2T_x$ sightly shifted to 550 cm^{-1}, which might be caused by disappearance of Al layer and the enlarged interlayer distance of MXene. When UiO-66–NH_2 was modified on $Ti_3C_2T_x$ nanosheets, due to the introduction of organic ligand, except

for the peak at 556 cm^{-1} ascribed to Ti_3C_2, the spectrum was dominated by the characteristic peaks of UiO-66–NH_2. After being calcined, all the peaks assigned to the organic components which were oxidized into CO_2 and H_2O during the calcination disappeared, leaving a strong peak at 458 cm^{-1} attributed to TiO_2 and a shoulder peak of ZrO_2 at 755 cm^{-1}. Finally, with the growth of Fe_3O_4, another shoulder peak at 574 cm^{-1} emerged. Raman and FT-IR characterization provided further verified the synthesis of MTMO.

The magnetic property of $MTMO_{3/4}$ was examined on a vibrating sample magnetometer to verify its viability for MSPE. As shown in Fig. 2D, $MTMO_{3/4}$ was superparamagnetic with a saturation magnetization of 26.3 emu•g^{-1}, which satisfy the demand of MSPE. From the inset picture, it is known that after 30 s in a magnetic field, MTMO can be separated from the liquid phase.

XPS and N_2 adsorption/desorption isotherm analyses were performed to obtain more comprehensive property information of $MTMO_{3/4}$. The spectra of $MTMO_{3/4}$ in Fig. S6 show characteristic peaks of Ti 2p, Zr 3d, Fe 2p, O 1s and C 1s, revealing the presence of these elements. Notably, carbon was also detected, might because the interference of the carbon-based conductive adhesive or that carbon was not completely removed during the calcination. According to the N_2 adsorption/desorption isotherm depicted in Fig. S7, BET area of $MTMO_{3/4}$ was 49.0 m^2•g^{-1}, which was close to other reported 2D materials [43,44].

3.2. Optimization of the parameters to synthesize MTMO

During the design and preparation process of MTMO, some conditions or parameters were optimized.

Different from the commonly-used MILD method [36], sonication was introduced in advance during each washing cycle replacing hand-shaking to accelerate the delamination process. Compared to the traditional MILD, this SA-MILD could not only save labor and time (hand-shake for minutes), but also increase the yield of MXene. As shown in Fig. S8, due to the high energy of sonication, the supernatant using SA-MILD protocol after each washing cycle was darker than that without sonication. And the supernatant turned opaquely black after 6 washing cycles. The yield of MXene using SA-MILD and traditional MILD was 84.9% ± 2.5% and 9.9% ± 0.5%, respectively, indicating the greatly higher efficiency of the delamination of $Ti_3C_2T_x$ nanosheets with the proposed SA-MILD method.

After that, in the process of in-situ growth of UiO-66–NH_2 onto $Ti_3C_2T_x$ nanosheets, different Ti/Zr was investigated. The amounts of $Ti_3C_2T_x$ MXene, $ZrCl_4$ and NH_2–BDC used for different ratios are listed in Table S1. The morphology of each synthesized Ti_3C_2–UiO-66–NH_2 was characterized by SEM. As shown in Fig. S9, when Ti/Zr was smaller than 1:2 (0:1, 1:4 and 1:3), UiO-66–NH_2 inclined to grow to larger crystals rather than spread on the surface of $Ti_3C_2T_x$ nanosheets. And when Ti/Zr was larger than 1:1 (2:1, 3:1 and 1:0), due to the lack of Zr source, not much of the surface of the nanosheets was covered by UiO-66–NH_2. When Ti/Zr was intermediate (1:2, 3:4 and 1:1), UiO-66–NH_2 nanocrystals grew uniformly on the surface of $Ti_3C_2T_x$ nanosheets.

XRD was used to characterize the structure of Ti_3C_2–UiO-66–NH_2. According to the XRD patterns of Ti_3C_2–UiO-66–NH_2 (Fig. S10), when Ti/Zr was larger than 1:1 (2:1, 3:1 and 1:0), peaks of UiO-66–NH_2 could hardly be seen, consistent with SEM results, where not many UiO-66–NH_2 nanocrystals could be seen. When Zr source used increased, due to the regular structure of MOF, strong diffraction peaks of UiO-66–NH_2 could be detected, confirming the formation of UiO-66–NH_2. Based on these results, ratios 1:2, 3:4 and 1:1 of Ti source to Zr source were selected for the following experiment.

To elucidate the mechanism of the combination of $Ti_3C_2T_x$ nanosheets and UiO-66–NH_2 nanocrystals, zeta potential of the synthesized Ti_3C_2–UiO-66–NH_2 was measured. As shown in Fig. S11, bare $Ti_3C_2T_x$ nanosheets (1:0) were negatively charged and UiO-66–NH_2 (0:1) was positively charged. As for Ti_3C_2–UiO-66–NH_2, all the zeta potentials were positive because the surface of $Ti_3C_2T_x$ nanosheets was covered by UiO-66–NH_2. With the dosage of Zr source increasing (Ti/Zr from 3:1 to 1:4), zeta potential of Ti_3C_2–UiO-66–NH_2 showed an increasing trend. This indicates that $Ti_3C_2T_x$ and UiO-66–NH_2 were combined by electrostatic interaction. To further verify this inference, Ti_3C_2–UiO-66 was synthesized under the same condition with Ti/Zr of 1:1, SEM images of which are shown in Fig. S12. It can be seen that $Ti_3C_2T_x$ nanosheets remained the relatively smooth surface after the reaction and UiO-66 nanoparticles leaned to agglomerating together rather than spreading on the surface of $Ti_3C_2T_x$ nanosheets. Besides, zeta potential of UiO-66 was measured to be −0.9 ± 0.8 mV. The loss of electrostatic interaction might be the reason why the MOF nanoparticles did not grow on the MXene nanosheets. These results further indicated that the combination of $Ti_3C_2T_x$ and UiO-66–NH_2 was driven by the opposite charges on their surfaces.

To investigate the proper calcination temperature, TG-DSC analysis was carried out for Ti_3C_2–UiO-66–$NH_{2(1/2)}$, Ti_3C_2–UiO-66–$NH_{2(3/4)}$ and Ti_3C_2–UiO-66–$NH_{2(1/1)}$. As shown in Fig. S13, all three Ti_3C_2–UiO-66–NH_2 started to lose the adsorbed moisture and organic solvent once being heated from the beginning. When the temperature went over 100 °C, the weight loss continued until the temperature reached 500 °C. This was because the organic component is not stable in air when heating, and the decomposition in the thermal process accelerated when the temperature increased and finally reached to an end when the temperature went up to 500 °C. According to the results, the calcination temperature was set to 500 °C. Noticeably, the remnant weight percentages of the three materials were 47.5%, 57.9% and 60.5%, respectively for Ti/Zr ratios of 1:2, 3:4 and 1:1. As the weight of $Ti_3C_2T_x$ increases when turning into TiO_2 while that of UiO-66–NH_2 decreases when turning into ZrO_2, lower Ti/Zr causes larger weight loss during the thermal process, with which the TG results agreed well.

3.3. Enrichment performance of MTMO towards phosphopeptides

In the first place, $MTMO_{1/2}$, $MTMO_{3/4}$ and $MTMO_{1/1}$ were all investigated for their performance in enriching phosphopeptides from the mixture of α-casein and β-casein digests. Water solutions containing 50% ACN and different volume ratios of TFA were used to optimize the acidity of the loading buffers. As shown in Figs. 3 and S14, S15, three MTMOs showed similar tendency when changing the TFA concentration in the loading buffer. When the TFA ratio was lower than 1.0%, although phosphopeptides could be detected, peaks of non-phosphopeptides were of high intensity and interfered with the identification of phosphopeptides, leading to information loss of them. When the TFA ratio reached 1% or 2%, the spectrum was predominated by the peaks of phosphopeptides, but still some peaks that does not belong to phosphopeptides were detected. When 5% of TFA was used, almost all the peaks of non-phosphopeptides were suppressed by those of phosphopeptides, giving the best acidity of the loading buffer. As exposing to strong acids might cause dissolution of the bare magnetite nanoparticles, and considering environmental friendliness at the same time, no higher ratio of TFA was investigated. The solution containing 5% TFA was chosen as the loading buffer. At the optimized loading buffer, comparing the spectra of three MTMOs, 22, 28 and 26 phosphopeptides or dephosphopeptides were identified after enrichment with $MTMO_{1/2}$, $MTMO_{3/4}$ and $MTMO_{1/1}$, respectively. Three materials showed comparable performance and $MTMO_{3/4}$ enriched a few more phosphopeptides, might because at the proper Ti/Zr, TiO_2 and ZrO_2 could maximize their synergistic effect together with Fe_3O_4. Therefore, $MTMO_{3/4}$ was chosen for the further exploration.

To investigate the effect of loading time on the enrichment performance towards phosphopeptides, pNPP was used as a model substance. As shown in Fig. S16, adsorption equilibrium was reached within 1 min, and the adsorption capacity of $MTMO_{3/4}$ to pNPP was calculated to be 31.6 mg•mL^{-1}. After that, loading time during the enrichment of phosphopeptides was also studied. To ensure the reach of adsorption equilibrium, also considering that the whole manual operation would

take a couple of minutes, 2, 5 and 10 min of the loading time were investigated. As shown in Fig. S17, no significant difference could be seen with the three different loading times, indicating that 2 min is enough for the equilibration.

The anti-interference ability of $MTMO_{3/4}$ was evaluated using the digest mixture of bovine α-casein, β-casein and BSA at different molar ratios (1:1:200, 1:1:500, 1:1:1000 and 1:1:2000). As shown in Fig. 4A and B, before enrichment, the peaks of phosphopeptides in the mixtures of the four molar ratios were hidden by the non-phosphopeptides of high concentration derived from BSA, and no peaks of phosphopeptides were detected. After enrichment, even though with the ratio of BSA went higher the MS spectra suffered more severe interference from the non-phosphopeptides, the peaks of phosphopeptides derived from $\alpha-/\beta$-casein could all be detected and take the dominance of the spectra after enrichment.

For the determination of sensitivity, $MTMO_{3/4}$ was further applied in different concentrations (1.0, 0.5, 0.2 and 0.1 nmol•L^{-1}) of $\alpha-/\beta$-casein digests. As shown in Fig. 4C and D, before enrichment, no peaks of phosphopeptides were detected. After enrichment, however, at a concentration of 1.0 nmol•L^{-1}, 16 peaks of phosphopeptides/dephosphopeptides were detected. Even when the concentration was as low as 0.1 nmol•L^{-1}, still 7 peaks assigned to phosphopeptides/dephosphopeptides could be identified, indicating the excellent sensitivity to phosphopeptides of the MTMO-based MSPE method.

The enrichment recovery of phosphopeptides by $MTMO_{3/4}$ was assessed using an isotope labeling method and a standard phosphopeptide (LRRA[*pS*]LGGK) was utilized as a model sample. As shown in Fig. S18 and Table S3, the recovery of the phosphopeptide was calculated to be 85.3%, indicating that $MTMO_{3/4}$ was competent to be an outstanding MSPE adsorbent for phosphopeptides.

3.4. Application in real samples

Non-fat milk was used to examine the applicability of $MTMO_{3/4}$ in the complex samples. As shown in Fig. S19, before enrichment, the spectrum was dominated by non-phosphopeptides peaks and only 7 phosphopeptides/dephosphopeptides were identified. After enrichment, however, 23 peaks assigning to phosphopeptides/dephosphopeptides could be identified, indicating the great enrichment efficiency of $MTMO_{3/4}$. The detailed information about the enriched phosphopeptides is summarized in Table S4.

To further verify the universal adaptability of $MTMO_{3/4}$, traditional Chinese medicine injections (TCMIs) were employed as additional real samples. TCMIs, composed of active substances from traditional Chinese medicines, have been widely used in research and clinical practice [45–47]. However, adverse drug reactions (ADRs), including acute allergic reactions, might occur in medication. Nevertheless, due to their complex components from natural materials including plants, animal products and minerals, the mechanism of how most TCMIs work or react with animal/human body remains unclear [48–50]. Among all the possible factors that cause ADRs, protein remnants from plants and animals could be dangerous if injected to animal/human body. Therefore, it is necessary to develop a reliable method for the analysis of proteins including phosphoproteins in TCMIs.

To evaluate the effects of the TCMI matrix, a mixture of α-casein and β-casein of 0.1 μmol•L^{-1} was spiked into QKLI or TRQI. Different ratios (0:1, 1:9, 1:3, 1:1, 3:1, and 1:0) of TCMI to water were investigated. As shown in Fig. 5, before enrichment, no matter QKLI (Fig. 5A) or TRQI (Fig. 5C) was investigated, when no TCMI was added in the matrix (ratio of 0:1), the spectra were dominated by non-phosphopeptides and only 5 peaks assigning to phosphopeptides were detected in each spectrum.

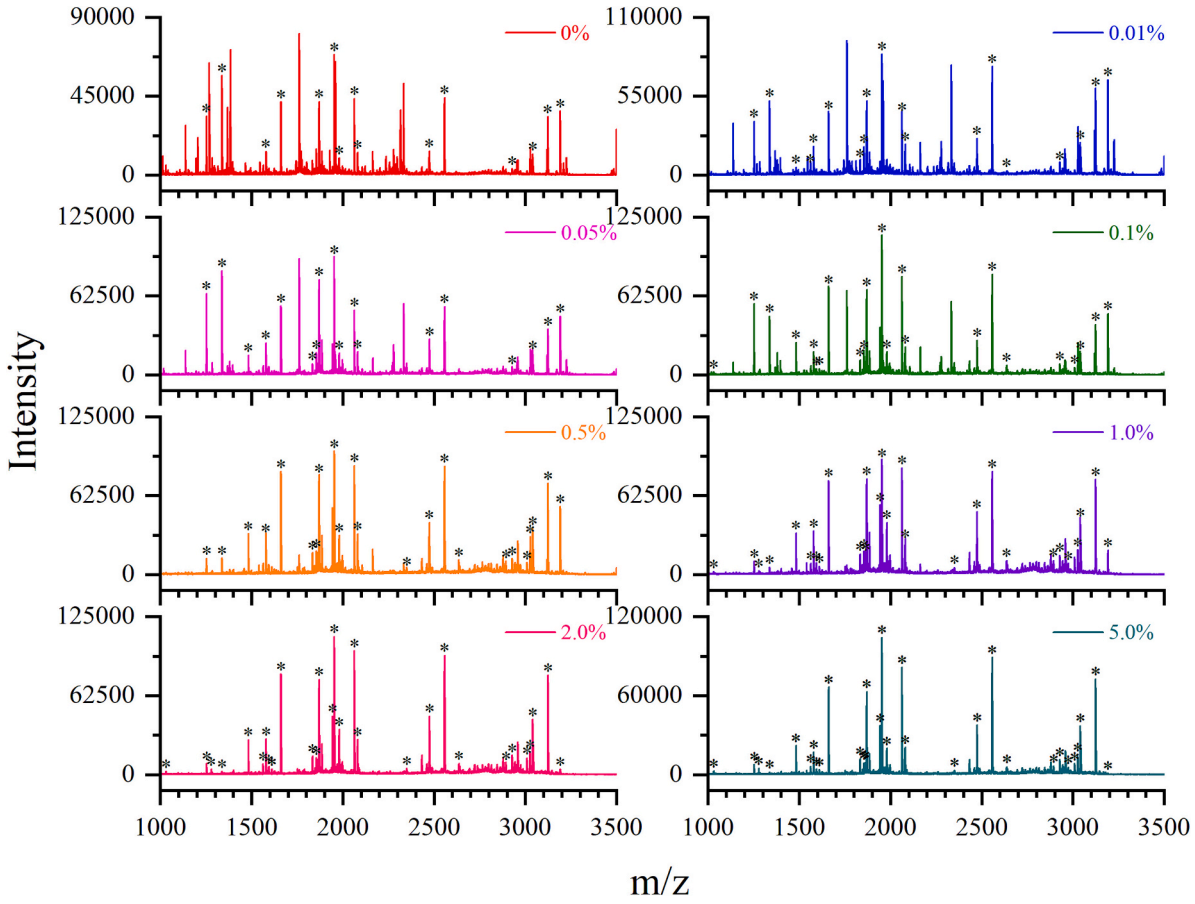

Fig. 3. MALDI-TOF MS spectra of $\alpha-/\beta$-casein digests after enrichment with $MTMO_{3/4}$ using water solutions containing different percentages of TFA as loading buffer.

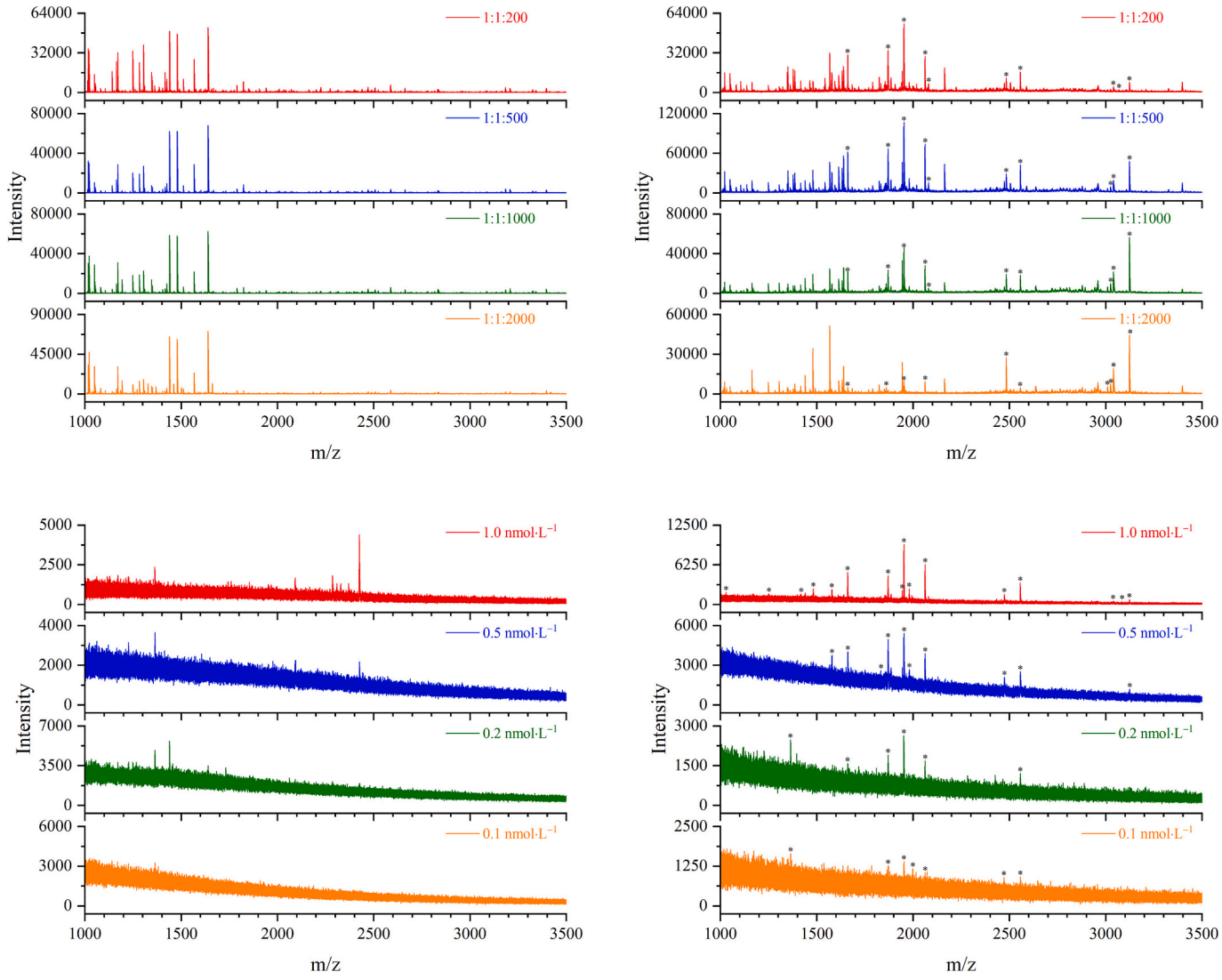

Fig. 4. MALDI-TOF MS spectra of $\alpha-/\beta$-casein and BSA digest mixture at different molar ratios before (A) and after (B) enrichment with $MTMO_{3/4}$, and MALDI-TOF MS spectra of $\alpha-/\beta$-casein digests of different concentrations before (C) and after (D) enrichment with $MTMO_{3/4}$.

With the addition of TCMI into the matrix, peaks of all peptides were getting suppressed by its complex components. When the ratio reached 1:1 or higher, most peaks including non-phosphopeptides and phosphopeptides disappeared in the spectra. After enrichment, no matter what the ratio of TCMI to water was, the spectra were dominated by phosphopeptides in both QKLI and TRQI matrices. When the ratio of 1:0 was investigated, suffering the interference of undiluted TCMI, the enrichment efficiency was affected. However, still 10 and 16 peaks of phosphopeptides/dephosphopeptides could be identified in QKLI and TRQI, respectively, indicating the strong ability of $MTMO_{3/4}$ to enrich phosphopeptides from complex samples. The detailed information about the enriched phosphopeptides from TCMIs is summarized in Table S4.

The limit of detection (LOD) of phosphopeptides were further determined in TCMIs. Different concentrations of α-casein and β-casein were spiked into QKLI and TRQI. As shown in Figs. S20 and S21, before enrichment, because of the interference of TCMI matrices, no peaks assigning to any peptides could be detected. After enrichment, when the concentration was 10 nmol•L^{-1}, 14 and 13 peaks assigning to phosphopeptides/dephosphopeptides were identified in QKLI and TRQI, respectively. With the concentration of $\alpha-/\beta$-casein decreasing, the peaks of phosphopeptides/dephosphopeptides identified decreased, too. Nevertheless, even when the concentration of $\alpha-/\beta$-casein was as low as 0.5 nmol•L^{-1}, 2 peaks of phosphopeptides could still be identified in both TCMIs, suggesting the high sensitivity of the enrichment of phosphopeptides from TCMIs with $MTMO_{3/4}$.

4. Conclusion

In conclusion, UiO-66–NH_2 nanoparticles were grown on $Ti_3C_2T_x$ nanosheets to form a potato-chip-like 2D MXene-MOF nanocomposites, and after being calcined, the 2D composites remaining original structure turned to L-TiO_2-ZrO_2 and satisfactory magnetism was endowed by an in-situ oxidation growth method of Fe_3O_4 nanoparticles. Notably, during the synthesis of the resulting magnetic trimetallic oxides (MTMOs), a sonication-assisted (SA) MILD method with high productive rate was proposed based on the conventional MILD method to delaminate $Ti_3C_2T_x$ into thin-layer nanosheets. Besides, a SISG method was developed, instead of solvothermal method for the in-situ uniform growth of UiO-66–NH_2 on $Ti_3C_2T_x$ MXene nanosheets. Furthermore, calcination in air allowed the MXene-MOF nanocomposites to form oxides, increasing the chemical stability of the composites and at the same time maintaining the abundant Ti—O and Zr—O sites. The Fe_3O_4 in situ loaded MTMOs could enrich phosphopeptides via facile MSPE separation format from biomedical samples in a short time with excellent selectivity, powerful anti-interference ability and high sensitivity. Profiting from the remaining of the potato-chip-like 2D structure, the binding

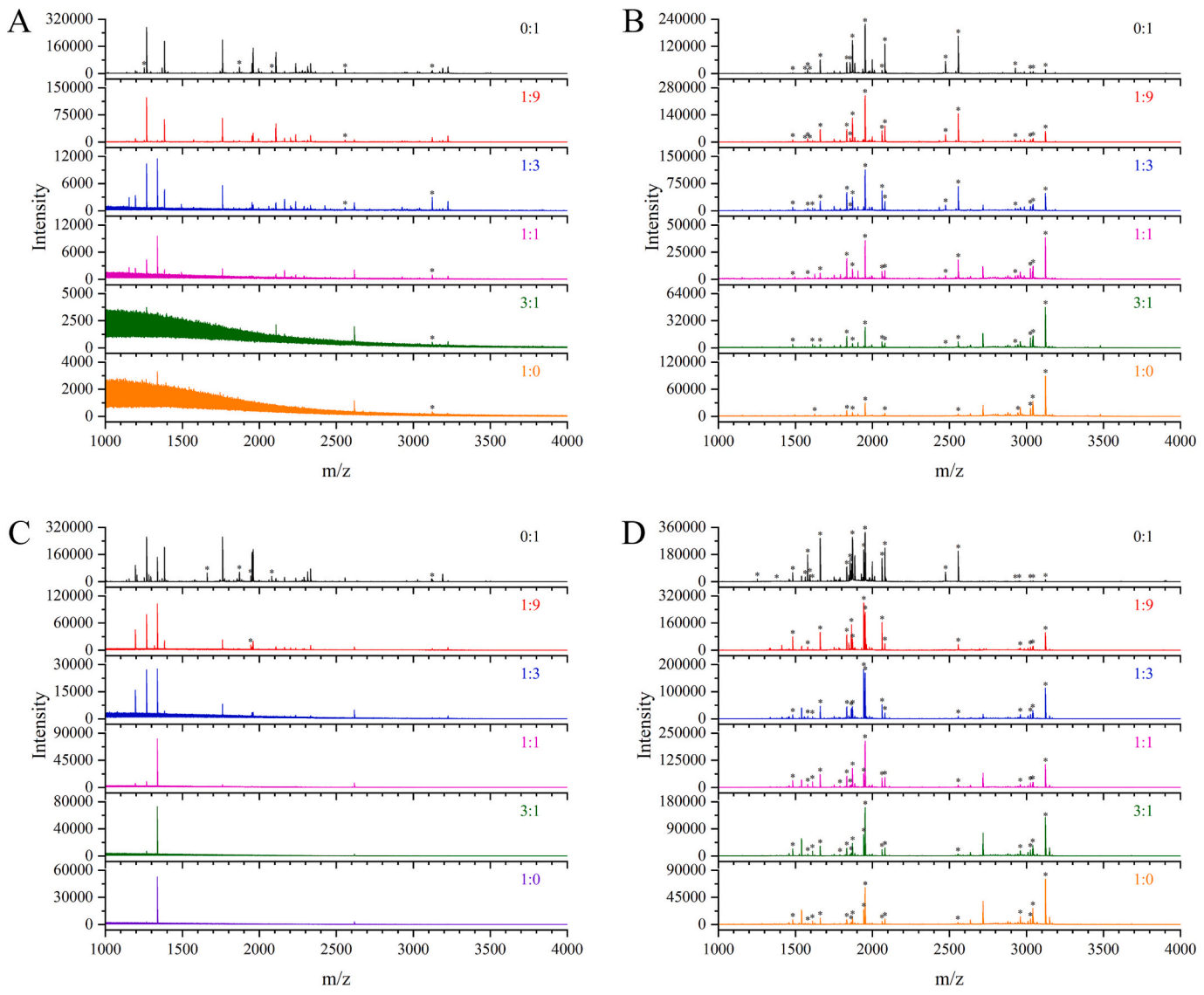

Fig. 5. MALDI-TOF MS spectra of digested $\alpha-/\beta$-casein spiking in different ratios of QKLI to water before (A) and after (B) enrichment with $MTMO_{3/4}$, and MALDI-TOF MS spectra of $\alpha-/\beta$-casein digests spiking in different ratios of TRQI to water before (C) and after (D) enrichment with $MTMO_{3/4}$.

sites for phosphopeptides were exposed sufficiently, favoring their mass transfer and shortening the interaction time towards MTMOs. Therefore, the MTMOs prepared based on SA-MILD and SISG could serve as a promising affinity material for MSPE or other potential forms of separation such as packed-solid-phase-extraction to fast and efficiently separate and enrich not only phosphopeptides but also various biomedical analytes in future peptidomic/proteomic studies.

CRediT authorship contribution statement

Sen Zhang: Writing – original draft, Visualization, Methodology, Investigation, Formal analysis, Data curation. **Xingdong Yang:** Visualization, Investigation, Formal analysis, Data curation. **Feng Zhang:** Visualization, Methodology, Data curation. **Jun-qin Qiao:** Visualization, Formal analysis, Data curation. **Wei-juan Zheng:** Visualization, Funding acquisition. **Hong-zhen Lian:** Writing – review & editing, Supervision, Resources, Project administration, Funding acquisition, Conceptualization.

Declaration of competing interest

The authors declare that they have no known competing financial interests or personal relationships that could have appeared to influence the work reported in this paper.

Acknowledgements

This work was supported by the National Natural Science Foundation of China (22176085, 22304075 and 21874065), and the National Key Research and Development Program of China (No. 2024YFF0618100).

Appendix A. Supplementary data

Supplementary data to this article can be found online at https://doi.org/10.1016/j.seppur.2025.135918.

Data availability

Data will be made available on request.

References

[1] M. Naguib, V.N. Mochalin, M.W. Barsoum, Y. Gogotsi, 25th anniversary article: MXenes: a new family of two-dimensional materials, Adv. Mater. 26 (2014) 992–1005.
[2] A.V. Mohammadi, J. Rosen, Y. Gogotsi, The world of two-dimensional carbides and nitrides (MXene), Science 372 (2021) 1165.
[3] Q.M. Peng, J.X. Guo, Q.R. Zhang, J.Y. Xiang, B.Z. Liu, A.G. Zhou, R.P. Liu, Y. J. Tian, Unique lead adsorption behavior of activated hydroxyl group in two-dimensional titanium carbide, J. Am. Chem. Soc. 136 (2014) 4113–4116.
[4] P. Zhang, M.X. Xiang, H.L. Liu, C.K. Yang, S.G. Deng, Novel two-dimensional magnetic titanium carbide for methylene blue removal over a wide pH range: insight into removal performance and mechanism, ACS Appl. Mater. Interfaces 11 (2019) 24027–24036.
[5] Q.R. Zhang, J. Teng, G.D. Zou, Q.M. Peng, Q. Du, T.F. Jiao, J.Y. Xiang, Efficient phosphate sequestration for water purification by unique sandwich-like MXene/magnetic iron oxide nanocomposites, Nanoscale 8 (2016) 7085.
[6] J.H. Zhu, J. Wang, Q. Liu, J. Yu, J.Y. Liu, R.R. Chen, D.L. Song, R.M. Li, J. Wang, Advanced MXene-based materials for efficient extraction of uranium from seawater and wastewater, Sci. Total Environ. 942 (2024) 173755.
[7] G.Y. Qing, Q. Lu, Y.T. Xiong, L. Zhang, H.X. Wang, X.L. Li, X.M. Liang, T.L. Sun, New opportunities and challenges of smart polymers in post-translational modification proteomics, Adv. Mater. 29 (2017) 1604670.
[8] A.M. Bode, Z. Dong, Post-translational modification of p53 in tumorigenesis, Nat. Rev. Cancer 4 (2004) 793–805.
[9] G. Simic, M.B. Leko, S. Wray, C. Harrington, I. Delalle, N. Jovanov-Milosevic, D. Bazadona, L. Buée, R. de Silva, G. Di Giovanni, C. Wischik, P.R. Hof, Tau protein hyperphosphorylation and aggregation in Alzheimer's disease and other tauopathies, and possible neuroprotective strategies, Biomolecules 6 (2016) 6.
[10] X.S. Li, B.F. Yuan, Y.Q. Feng, Recent advances in phosphopeptide enrichment: strategies and techniques, TrAC-trends, Anal. Chem. 78 (2016) 70–83.
[11] B. Eyrich, A. Sickmann, R.P. Zahedi, Catch me if you can: mass spectrometry-based phosphoproteomics and quantification strategies, Proteomics 11 (2011) 554–570.
[12] P.J. Boersema, S. Mohammed, A.J.R. Heck, Phosphopeptide fragmentation and analysis by mass spectrometry, J. Mass Spectrom. 44 (2009) 861–878.
[13] J.J. Li, S.Q. Wen, B. Li, N. Li, X.Q. Zhan, Phosphorylation-mediated molecular pathway changes in human pituitary neuroendocrine tumors identified by quantitative phosphoproteomics, Cells 10 (2021) 2225.
[14] G. Hardman, S. Perkins, P.J. Brownridge, C.J. Clarke, D.P. Byrne, A.E. Campbell, A. Kalyuzhnyy, A. Myall, P.A. Eyers, A.R. Jones, C.E. Eyers, Strong anion exchange-mediated phosphoproteomics reveals extensive human non-canonical phosphorylation, EMBO J. 38 (2019) e100847.
[15] R.Z. Tang, Q. Bai, S.J. Ma, J.J. Ou, Materials, workflows and applications of IMAC for phosphoproteome profiling in the recent decade: a review, TrAC-Trends Anal. Chem. 158 (2023) 116862.
[16] J.-Y. Li, Z.-M. Cao, Y. Hua, W. Gao, X.-Z. Yu, W.-B. Shang, H.-Z. Lian, Solvothermal synthesis of novel magnetic nickel based iron oxide nanoparticles for selective capture of global- and mono-phosphopeptides, Anal. Chem. 92 (2020) 1058–1067.
[17] B.C. Wang, Z.H. Xie, C.-F. Ding, C.H. Deng, Y.H. Yan, Recent advances in metal oxide affinity chromatography materials for phosphoproteomics, TrAC-Trends Anal. Chem. 158 (2023) 116881.
[18] X.W. Li, N. Zhang, R.Z. Tang, J.W. Lyu, Z. Liu, S.J. Ma, J.J. Ou, M.L. Ye, Comparative evaluation of MAX-Ti_3AlC_2 and MXene-Ti_3C_2 as affinity chromatographic materials for highly selective enrichment of phosphopeptides, Nanoscale 13 (2021) 2923–2930.
[19] L.Z. Yu, B. Luo, X.X. Zhou, Y.C. Liu, F. Lan, Y. Wu, In situ controllable fabrication of two-dimensional magnetic Fe_3O_4/TiO_2@$Ti_3C_2T_x$ composites for highly efficient phosphopeptides enrichment, ACS Appl. Mater. Interfaces 13 (2021) 54665–54676.
[20] L.Z. Yu, J. He, S. Yan, Y.C. Liu, F. Lan, Y. Wu, Magnetic MXene/PAMAM composites with flexible dimensional regulation for highly effective enrichment of phosphopeptides, ACS Sustain. Chem. Eng. 10 (2022) 2494–2508.
[21] J. He, L.Z. Yu, B. Luo, Y.C. Liu, F. Lan, Y. Wu, Dielectric barrier discharge induced Oxid-$Ti_3C_2T_x$/UiO-66–NH_2 composites for efficient phosphopeptides enrichment, Mater. Design 233 (2023) 112193.
[22] S. Zhang, J.-Y. Li, W. Gao, J.-Q. Qiao, H.-Z. Lian, Magnetic Ti_3C_2 MXene nanosheets prepared for enrichment of phosphopeptides, ACS Appl. Mater. Interfaces 15 (2023) 16505–16514.
[23] Y.C. Liu, B. Luo, Z.Y. Li, S.X. Shui, L.Z. Yu, Y. Wu, Metal-phenolic networks modified two-dimensional magnetic MXene-based composites for highly efficient enrichment of phosphopeptides, Microchem. J. 193 (2023) 109114.
[24] F.F. Xu, D.Y. Shang, C.C. Zhu, G.Z. Du, J.S. Shi, X.F. Dong, X.L. Li, X.M. Liang, In situ MXene controlled synthesis of polycrystalline TiO_2 for highly efficient enrichment of phosphopeptides, ACS Appl. Mater. Interfaces 17 (2025) 260–268.
[25] W.B. Zhao, Y.T. Zeng, Y.H. Zhao, X.L. Wu, Recent advances in metal-organic framework-based electrode materials for supercapacitors: a review, J Energy Storage 62 (2023) 106934.
[26] J.-Y. Li, S. Zhang, W. Gao, Y. Hua, H.-Z. Lian, Guanidyl-functionalized magnetic bimetallic MOF nanocomposites developed for selective enrichment of phosphopeptides, ACS Sustain. Chem. Eng. 8 (2020) 16422–16429.
[27] Z. Dong, Y.Y. Xin, B.W. Xiang, R.L. Yang, M.L. Zhu, B.L. Cui, C.J. Xie, S.S. Long, W. W. Zhou, J.W. Liu, L.B. Qian, H.Z. Guo, Y.P. Zheng, Z.Y. Yang, D.C. Wang, Interface layer-assisted construction of metal organic framework based porous liquids for high performance CO_2 selective separation, J. Environ. Chem. Eng. 13 (2025) 119292.
[28] Z. Dong, Y.Y. Xin, B.W. Xiang, B.L. Cui, R.L. Yang, W.W. Zhou, J.W. Liu, J.D. Li, S. S. Long, L.B. Qian, X.X. Che, J.W. Fan, Z.Y. Yang, Y.P. Zheng, D.C. Wang, Type III porous liquids based on UiO-66 modified by growing the silica layer for CO_2 selective separation, Sep. Purif. Technol. 377 (2025) 134502.
[29] K. Chattopadhyay, M. Mandal, D.K. Maiti, A review on zirconium-based metal-organic frameworks: synthetic approaches and biomedical applications, Mater. Adv. 5 (2024) 51–67.
[30] M. Wu, Q. Zhang, Q.Y. Zhang, H. Wang, F.W. Wang, J.M. Liu, L.Q. Guo, K. Song, Research progress of UiO-66-based electrochemical biosensors, Front. Chem. 10 (2022) 842864.
[31] H.B. Li, J.L. Li, L. Ma, X.L. Zhang, J.F. Li, J.B. Li, T. Lu, L.K. Pan, Heteroatomic interface engineering of an octahedron VSe_2–ZrO_2/C/MXene composite derived from a MXene hybrid as a superior-performance anode for lithium-ion batteries, J Mater Chem A 11 (2023) 2836.
[32] H. He, X.S. Wang, Q. Yu, W.B. Wu, X.Y. Feng, D.Y. Kong, X.H. Ren, J.K. Gao, In situ growth of Ti_3C_2/UiO-66-NH_2 composites for photoreduction of Cr(VI), Catalysts 13 (2023) 876.
[33] M.H. Afzal, W. Pervaiz, Z. Huang, Z.Y. Wang, G.F. Li, H.F. Liu, In situ synthesis of a UiO-66–NH_2@Ti_3C_2 composite for advanced electrochemical detection of acetaminophen, Nanoscale 17 (2025) 4444.
[34] H.S. Far, M. Najafi, E. Moradi, M. Atighi, M. Rabbani, M. Hasanzadeh, Metal-organic frameworks decorated $Ti_3C_2T_x$ MXene nanosheets (MXene@UIO-66) for enhanced photocatalytic dye degradation, J. Mol. Struct. 1312 (2024) 138627.
[35] H.M. Deng, H.S. Gu, Structure regulation of two-dimensional lamellar NH_2–UiO-66@MXene membrane for efficient H_2/CO_2 separation, J CO_2 Util 83 (2024) 102796.
[36] M. Alhabeb, K. Maleski, B. Anasori, P. Lelyukh, L. Clark, S. Sin, Y. Gogotsi, Guidelines for synthesis and processing of two-dimensional titanium carbide ($Ti_3C_2T_x$ MXene), Chem. Mater. 29 (2017) 7633–7644.
[37] M. Downes, C.E. Shuck, B. McBride, J. Busa, Y. Gogotsi, Comprehensive synthesis of $Ti_3C_2T_x$ from MAX phase to MXene, Nat. Protoc. 19 (2024) 1807–1834.
[38] X. Ma, L. Wang, Q. Zhang, H.-L. Jiang, Switching on the photocatalysis of metal-organic frameworks by engineering structural defects, Angew. Chem. Int. Ed. 58 (2019) 12175–12179.
[39] V. Presser, M. Naguib, L. Chaput, A. Togo, G. Hug, M.W. Barsoum, First-order Raman scattering of the MAX phases: Ti_2AlN, $Ti_2AlC_{0.5}N_{0.5}$, Ti_2AlC, $(Ti_{0.5}V_{0.5})_2AlC$, V_2AlC, Ti_3AlC_2, and Ti_3GeC_2, J. Raman Spectrosc. 43 (2012) 168–172.
[40] A. Sartcheva, Y. Gogotsi, Raman spectroscopy analysis of the structure and surface chemistry of $Ti_3C_2T_x$ MXene, Chem. Mater. 32 (2020) 3480–3488.
[41] I. Strauss, K. Chakarova, A. Mundstock, M. Mihaylov, K. Hadjiivanov, N. Guschanski, J. Caro, UiO-66 and UiO-66–NH_2 based sensors: dielectric and FTIR investigations on the effect of CO_2 adsorption, Microporous Mesoporous Mater. 302 (2020) 110227.
[42] S.N. Basahel, T.T. Ali, M. Mokhtar, K. Narasimharao, Influence of crystal structure of nanosized ZrO_2 on photocatalytic degradation of methyl orange, Nanoscale Res. Lett. 10 (2015) 73.
[43] F.Y. Kong, X.D. He, Q.Q. Liu, X.X. Qi, D.D. Sun, Y.T. Zheng, R.G. Wang, Y.L. Bai, Further surface modification by carbon coating for in-situ growth of Fe_3O_4 nanoparticles on MXene Ti_3C_2 multilayers for advanced Li-ion storage, Electrochim. Acta 289 (2018) 228–237.
[44] L.B. Wang, H. Liu, X.L. Lv, G.Z. Cui, G.X. Gu, Facile synthesis 3D porous MXene $Ti_3C_2T_x$@RGO composite aerogel with excellent dielectric loss and electromagnetic wave absorption, J. Alloys Compd. 828 (2020) 154251.
[45] X.R. Lou, H. Chen, N. Shi, R.X. Yu, S.L. Li, Y. Yang, S.Q. Liu, J.F. Xie, H.B. Qiu, Treatment effects of Xuebiqing injection in patients with sepsis by clinical phenotype: a post hoc analysis of the EXIT-SEP trial, eClinicalMedicine 86 (2025) 103341.
[46] X.Y. Zhang, X.Y. Lao, S.C. Liao, C.Y. Ye, C. Wang, Efficacy of Shenkang injection combined with renin-angiotensin-aldosterone system blockers in diabetic nephropathy: a systematic review and meta-analysis of randomized controlled trials, Ren. Fail. 47 (2025) 2499231.
[47] S.C. Li, Y.Q. Wang, X.Y. Sun, L.Y. Lu, Y. Yong, X.N. Kong, J.A. Song, Suppressing neuroinflammation by Shenfu injection against ischemic stroke in mice via inhibiting RAGE-PI3K-Akt pathway, Phytomedicine 144 (2025) 156940.
[48] W. Zhuang, G. Sun, X.L. Lin, B. Chen, L. Wu, D.C. Jiang, S.Y. Xi, Medication with caution: analysis of adverse reactions caused by a combination of Chinese medicine and warfarin sodium tablets, J. Ethnopharmacol. 254 (2020) 112586.
[49] X.B. Zhu, M. Guo, Z.H. Zhang, L.H. Sun, L. Liu, L.J. Zhou, C.L. Shan, Y. Yang, L. D. Kan, L.C. Li, Chinese herbal injections for coronavirus disease 2019 (COVID-19): a narrative review, Integr. Med. Res. 10 (2021) 100778.
[50] R. Zheng, L.Y. Tao, J.S.W. Kwong, C.M. Zhong, C.Y. Li, S.Q. Chen, Y. Sun, X. Y. Zhang, H.C. Shang, Risk factors associated with the severity of adverse drug reactions by Xiyanping injection: a propensity score-matched analysis, J. Ethnopharmacol. 250 (2020) 112424.